The Astrophysical Journal, 968:127 (15pp), 2024 June 20 https://doi.org/10.3847/1538-4357/ad41b5
© 2024. The Author(s). Published by the American Astronomical Society.
OPEN ACCESS

Stellar Abundances at the Center of Early-type Galaxies with Fine Structure

Nicholas Barth[1], George C. Privon[1,2,3], Rana Ezzeddine[1], Aaron S. Evans[2,3], and Ezequiel Treister[4]
[1] Department of Astronomy, University of Florida, 1772 Stadium Road, Gainesville, FL 32611, USA
[2] National Radio Astronomy Observatory, 520 Edgemont Road, Charlottesville, VA 22903, USA
[3] Department of Astronomy, University of Virginia, 530 McCormick Road, Charlottesville, VA 22904, USA
[4] Instituto de Astrofísica, Facultad de Física, Pontificia Universidad Católica de Chile, Campus San Joaquín, Av. Vicuña Mackenna 4860, Macul Santiago, 7820436, Chile
Received 2023 September 25; revised 2024 April 5; accepted 2024 April 18; published 2024 June 20

Abstract

Our understanding of early-type galaxies (ETGs) has grown in the past decade with the advance of full-spectrum fitting techniques used to infer the properties of the stellar populations that make up the galaxy. We present ages, central velocity dispersions, and abundance ratios relative to Fe of C, N, O, Mg, Si, Ca, Ti, Cr, Mn, Co, Ni, Cu, Sr, Ba, and Eu, derived using full-spectrum fitting techniques for three ETGs, NGC 2865, NGC 3818, and NGC 4915. Each of these three galaxies were selected because they have optical, disturbed structures (fine structure) that are linked to major merger events that occurred 1, 7, and 6 Gyr ago, respectively. Two of the ETGs, NGC 3818 and NGC 4915, show chemical signatures similar to ETGs without fine structure, which is consistent with a gas-poor merger of elliptical galaxies in which substantial star formation is not expected. For NGC 2865, we find a statistically higher abundance of Ca (an α element) and Cr and Mn (Fe-peak elements). We show that for NGC 2865, a simple gas-rich merger scenario fails to explain the larger abundance ratios compared to ETGs without fine structure. These three ETGs with fine structure exhibit a range of abundances, suggesting ETGs with fine structure can form via multiple pathways and types of galaxy mergers.

Unified Astronomy Thesaurus concepts: Early-type galaxies (429); Chemical abundances (224); Chemical enrichment (225); Spectroscopy (1558)

Supporting material: figure set

1. Introduction

The chemical abundance ratios of galaxies are powerful tools for constraining the evolution processes and formation channels that galaxies experience over their cosmic lifetime (Maiolino & Mannucci 2019; Feldmeier-Krause et al. 2021). Early-type galaxies (ETGs) have two main stages of formation: an early ($z \sim 2$) collapse of gas, forming stars in a compact core, or an ongoing second stage where satellite galaxies are accreted and ex situ form stars (Naab et al. 2009, Oser et al. 2010). The fraction of ETGs that show recent star formation is low ($\sim$10%), and it has been suggested that the increases in recent star formation could be a result of galaxy interactions and merger activity in the past few billion years (Greif et al. 2010, Urrutia-Viscarra et al. 2017).

With little-to-no star formation occurring in ETGs, the integrated light from these systems is dominated by old stellar populations. Through full spectral fitting, we could learn about how the ETGs were assembled and what the early star formation period looked like (Feldmeier-Krause et al. 2021). The chemical abundance ratios derived for the ETGs' stellar populations point to chemical-enrichment events, and are a powerful tool in untangling the chemical evolution within the galaxy. Beginning with the α elements (e.g., C, N, O, Mg, Si, Ca, Ti), these are produced via massive ($>8\ M_{\odot}$) stars undergoing core-collapse supernovae (CCSNe). Fe-peak elements are formed later, as Type Ia supernovae (SNe) start to occur within the stellar populations. The delay between when CCSNe dominate and when Type Ia SNe dominate is represented by the abundance ratios of elements formed in each event (e.g., [α/Fe], where α elements are formed in CCSNe and Fe is formed in Type Ia SNe). The abundance ratios thus can point to characteristics of the star formation history of a galaxy (Feldmeier-Krause et al. 2021).

Some spectroscopic galactic surveys, such as the ATLAS3D and MASSIVE surveys, have widely improved our knowledge of the chemical composition of ETGs through the study of the absorption and emission features in their spectra (Cappellari et al. 2010, Ma et al. 2014). Such surveys have defined trends showing how ETGs' chemical abundances correlate with their ages and masses, with more massive ETGs showing higher metallicities, higher α-element abundances, and older stellar populations. However, many of these surveys specifically target ETGs with unperturbed light profiles (i.e., lacking stellar features such as tails, shells, or streams, also known as fine structure) to study the early Universe and to remove dynamical and chemical effects that took place at later epochs. The trends in the chemodynamical properties of ETGs with fine structure have not been as widely studied as a result, and it is not obvious that ETGs with fine structure would share the same characteristics of ETGs without fine structure. The type of fine structure present in ETGs is indicative of the type of merger (gas-rich versus gas-poor merger, major versus minor merger, etc.; Schweizer et al. 1990; Schweizer & Seitzer 1992; Giri et al. 2023), and thus with our study of stellar populations within ETGs with fine structure we are able to link the type of merger to any chemical evolution history of the galaxies.

Our analysis of ETGs with fine structure begins with a description of our targets and observations in Section 2. We describe the full-spectrum fitting method used to determine

Original content from this work may be used under the terms of the Creative Commons Attribution 4.0 licence. Any further distribution of this work must maintain attribution to the author(s) and the title of the work, journal citation and DOI.

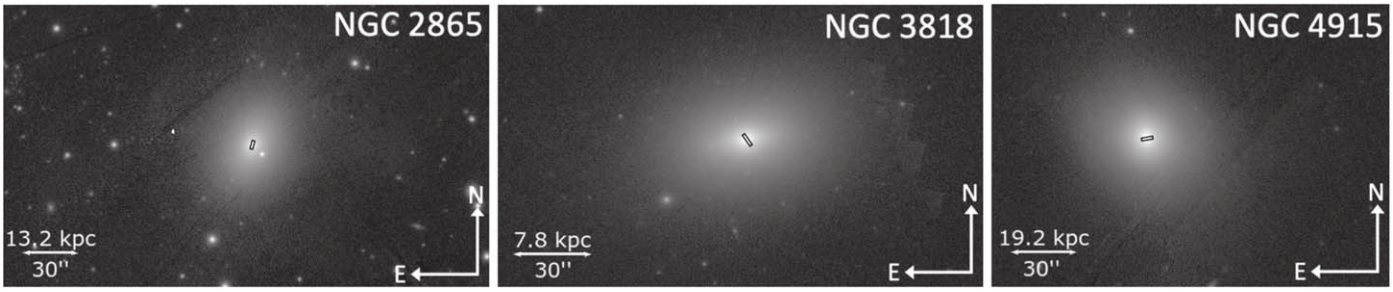

Figure 1. Slit coverage for NGC 2865, NGC 3818, and NGC 4915. The black box at the center of each galaxy represents the $1'' \times 5''$ slit used in the observations taken with the MIKE spectrograph. Images of each galaxy were taken from the Pan-STARRS Data Release 1 survey (in the z band; Chambers et al. 2016).

Table 1
Our Program Target ETGs

Galaxy (1)	Redshift (2)	Morph. Type (3)	Σ (4)	$\tau_{\rm merger}$ (5)	$\log_{10} M_*$ (6)	$(U-B)$ (7)	$(B-V)$ (8)
NGC 2865	0.008	E3	6.4	~1 Gyr	10.5	0.42	0.91
NGC 3818	0.005	E5	1.30	~7 Gyr	10.65	0.48	0.96
NGC 4915	0.01	E0	5.48	~6 Gyr	10.52	0.47	0.94

Note. Column (1): Galaxy ID; column (2): redshift (Smith et al. 2000); column (3): Hubble morphological type (de Vaucouleurs et al. 1991); column (4) fine-structure parameter (Schweizer et al. 1990, Schweizer & Seitzer 1992); column (5): time since last merger (in billions of years; Schweizer et al. 1990, Schweizer & Seitzer 1992); column (6): estimated stellar mass (in solar masses; Fukazawa et al. 2006); columns (7) and (8): observed colors (Schweizer et al. 1990).

chemodynamical parameters for each galaxy in Section 3. We present our results of the fitting in Section 4, which include ages, velocity dispersions, and chemical abundance ratios for each ETG. We describe how our results compare to ETGs without fine structure in Section 5. Finally, we discuss and summarize our conclusions in Sections 6 and 7, respectively.

2. Targets and Observations

2.1. Target Selection

Three ETGs were selected for high-resolution observations, NGC 2865, NGC 3818, and NGC 4915. Each target shows evidence of a major merger through photometric observations of fine structure. NGC 3818 and NGC 4915 were studied in Schweizer et al. (1990) and Schweizer & Seitzer (1992), who found a correlation between fine structure and the line strengths and *UBV* colors of ETGs. The *UBV* colors, used to derive a heuristic merger age for the ETGs, show that galaxies with a larger amount of fine structure have had more recent (within 1–7 Gyr) major mergers. Schweizer et al. (1990) define the fine-structure parameter, Σ, as

$$\Sigma = S + \log(1 + n) + J + B + X, \quad (1)$$

where S is the visual estimate of the strength of the ETG's ripples, n is the number of detected ripples, J is the number of plumes, streams, or tails of luminous material, B is the visual estimate of the boxiness of the isophote fit to the ETG's light profile, and X indicates the absence or presence of an X structure. Σ was defined as a rough measurement of dynamical youth or rejuvenation (Schweizer & Seitzer 1992). Further studies have found that the type of fine structure found in a merger remnant is indicative of the type of merger it underwent (Giri et al. 2023).

NGC 2865 is an E3 galaxy, originally studied in Jorgensen et al. (1992). Further observations conducted by Rampazzo et al. (2007) found fine structure that indicated a recent merger history. It has the highest fine-structure content ($\Sigma = 6.4$) among the three ETGs, with extended tidal tails and shells surrounding the galaxy. Fort et al. (1986) reports that NGC 2865's shells contribute 11%–22% of the total luminosity and have colors that resemble disk galaxies. NGC 2865 is thought to have a young, central stellar component formed within the last billion years and a kinematically distinct core (Longhetti et al. 1999; Hau & Forbes 2006; Rawle et al. 2010).

NGC 3818 is a bulge-dominated E5 galaxy, with a disk fully embedded in a boxy bulge and the least amount of fine structure out of the three ETGs (Scorza & van den Bosch 1998). NGC 3818 is located in a low-density environment (density of galaxies brighter than $M_B = -16$ is 0.2) in the Crater Cloud group of galaxies (Tully 1988). Panuzzo et al. (2011) studied mid-infrared spectra of NGC 3818 and determined it as a passive ETG, with no emission lines in its spectra, indicating little-to-no current activity within the galaxy.

NGC 4915 is a relatively isolated E0 galaxy thought to have formed <7 Gyr ago (Schweizer & Seitzer 1992). At its center, NGC 4915 hosts a young stellar population that has a strong Hβ absorption feature (Schweizer & Seitzer 1992). Strong Balmer features, such as the Hβ line, point to A or F stars added to an old stellar population, which is consistent with an aging starburst population that formed during the merger. Schweizer & Seitzer (1992) describes the fine structure around NGC 4915 to be extremely boxy, with an apparent X structure.

2.2. Observations

The observations of NGC 2865, NGC 3818, and NGC 4915 were obtained on 2016 May 3, using the Magellan Inamori Kyocera Echelle (MIKE) double-echelle spectrograph located on the MAGELLAN 6.5 m Clay telescope (Bernstein et al. 2003). Each exposure was taken with 3×2 binning using a $1'' \times 5''$ single slit, resulting in a resolving power of $R \sim 28{,}000$ in the blue arm of MIKE and a $R \sim 22{,}000$ in the red arm. Figure 1 shows the central slit coverage for each galaxy with respect to the galaxy as a whole. With a $2.2''$ extraction

Table 2
Prior Limits Set in This Work for the ALF Fitting Routine

Parameter	Low Prior	High Prior
σ (km s^{-1})	20.0	600.0
Age (Gyr)	2.0	13.5
Age of young SSP (Gyr)	0.5	3.0
log (Mass % of young SSP)	−6.0	−0.5
[Fe/H]	−0.4	0.5
[O/Fe]	−1.0	0.6
[C/Fe]	−1.0	0.5
[N/Fe]	−1.0	0.5
[Mg/Fe]	−0.4	0.5
[Si/Fe]	−0.5	0.5
[Ca/Fe]	−0.5	0.5
[Ti/Fe]	−1.0	0.5
[Cr/Fe]	−0.5	0.5
[Mn/Fe]	−0.3	1.0
[Co/Fe]	−0.5	0.5
[Ni/Fe]	−1.0	0.5
[Cu/Fe]	−0.5	0.5
[Sr/Fe]	−1.0	1.0
[Ba/Fe]	−1.0	1.0
[Eu/Fe]	−1.0	1.0

aperture, using the distances derived from the redshift listed in Table 1, we obtain a spatial coverage of 0.2×0.4, 0.1×0.2, and 0.2×0.5 kpc for NGC 2865, NGC 3818, and NGC 4915, respectively. Each galaxy had three 1500 s exposures, with the exception of NGC 4915, whose last exposure was cut short at 800 seconds due to time constraints.

We used the `CarPy` data-reduction pipeline to combine, correct, and wavelength calibrate the observations of each galaxy (Kelson et al. 2000; Kelson 2003). Each spectrum was shifted to the rest frame from the observed frame by using the galaxies' recorded redshift, listed in Table 1. The resulting spectra covered a rest-frame wavelength range of ∼3300–9200 Å.

3. Chemical Analysis

3.1. Full Spectral Fitting

We fit the spectra of the three ETGs using the Absorption Line Fitter (ALF), a simple stellar population (SSP) fitting method developed by Conroy & van Dokkum (2012a). ALF utilizes both synthetic and empirical stellar libraries to create a grid of SSP models used to fit integrated-light spectra of galaxies (Conroy & van Dokkum 2012b). In order to explore the large parameter space defined by the prior bounds, ALF uses a Monte Carlo Markov Chain (MCMC) fitting routine that produces models with various parameter combinations and uses a χ^2 minimization to determine the best-fitting model.

ALF's full capabilities include the ability to determine the abundance ratios of 19 elements, kinematic properties such as recessional velocity and velocity dispersion, and an age and mass fraction of a subdominant, younger stellar population. We apply ALF to our target galaxies to determine the parameters of the light-dominating stellar population at the center of each galaxy with priors for each parameter listed in Table 2, and we fix the initial mass function (IMF) to a Kroupa IMF (Kroupa 2001). After each fitting run by ALF, we check the posterior distributions of each parameter to make sure that the MCMC walkers are not settling on a value at the prior edge.

Conroy et al. (2014) show the residuals to their fitting procedure of stacked, high-SNR Sloan Digital Sky Survey (SDSS) galaxy spectra. They note that certain wavelength regions of their spectra show a correlation between galaxies' velocity dispersions and the residuals, indicating that there are unknown factors that affect those regions that are not accounted for by ALF. As a result of this uncertainty, we chose to mask regions that showed correlations with the velocity dispersion in the Conroy et al. (2014) stacked SDSS data when fitting our galaxies with ALF.

Additionally, the major Na line used in the fitting routine is the NaD doublet at 5900 Å, which is heavily influenced by the interstellar medium (ISM) Na. Since the NaD line is the only strong Na source in our spectra, we risk fitting models with inflated Na abundances due to contributions from both stellar photospheres and ISM absorption. As such, we mask the NaD line from our fit and do not report a stellar Na abundance here.

Figures 2(a)–(c) show our best-fit models to each ETG. We fit the wavelength regions 4000–6800 Å and 8400–8700 Å, taking care to mask regions affected by atmospheric and galaxy emission lines. The residual percentage between our best-fit model and the data is also shown, with a range of ±10%.

4. Results

4.1. Stellar Population Parameters

The stellar population parameters of our analysis of NGC 2865, NGC 3818, and NGC 4915 are listed in Table 3. Figure 3 shows our fitted age and [Fe/H] values as a function of central velocity dispersion compared to other literature samples of ETGs. ALF fits an element X with respect to hydrogen, and to transform this ratio with respect to iron, we subtract the fitted [Fe/H] measurement ($[X/Fe] = [X/H] - [Fe/H]$). Additionally, certain elements must be corrected with theoretical response functions. These response function abundance corrections come from synthetic stellar libraries and supplement areas of the spectra where the empirical model library fails to capture the contributions from various elements (Conroy & van Dokkum 2012b; Conroy et al. 2018). As a result, the elements O, Mg, Ca, Si, and Ti are corrected based off relations derived in Schiavon (2007), Bensby et al. (2014), and Milone et al. (2011). Conroy et al. (2018) found that the empirical library abundances for C, N, Na, V, Cr, Mn, Co, Cu, Ba, Sr, and Eu were close to zero for a wide metallicity range ($[X/Fe]_{lib}[Z/H] = 0$), indicating that no additional abundance was needed to add to the theoretical response function for these elements. The bottom panels of the figures in the Appendix show where each element can have an effect on the spectra in the observed wavelength region. By fitting the entire spectrum we are able to constrain abundances of elements using their combined impact on the integrated light. In the case of O, which does not have individual lines in our spectra, we derive an O abundance using the contributions from molecules that include O (such as H_2O, TiO, MgO, AlO, VO, CO, OH, and SiO) and produce an absorption features in the response function.

As shown in Figure 3, we derive a younger stellar population for NGC 2865 at ∼3.9 Gyr, while we obtain relatively older derived stellar populations of ∼7.3 and ∼6.0 Gyr for NGC 3818 and NGC 4915, respectively. We also show comparisons of ages to stacked SDSS galaxies (Conroy & van Dokkum 2012b), LRIS galaxies (Conroy & van Dokkum 2012b), the

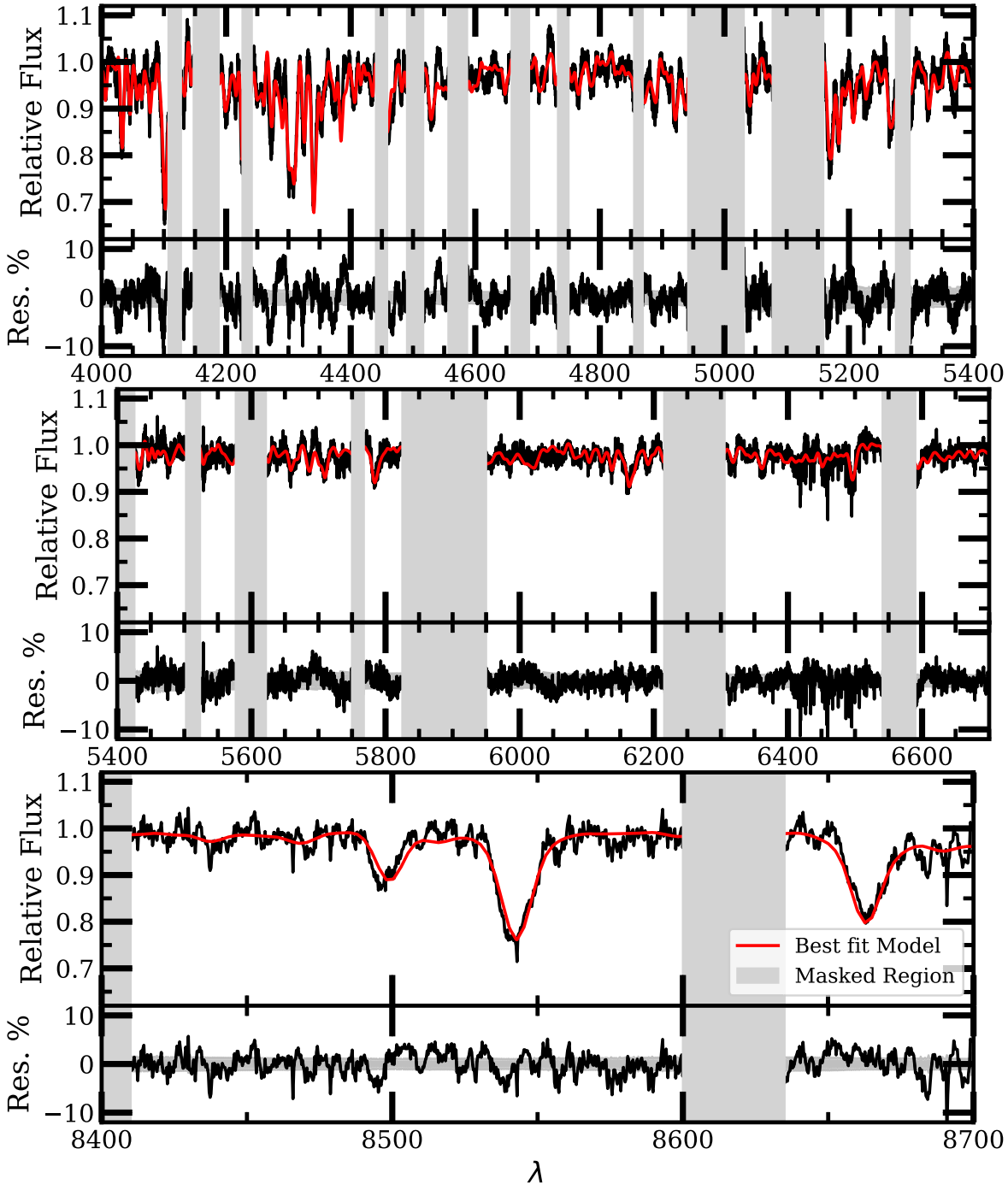

Figure 2. (a) Top: comparison of the fitted model (red) to the observed spectrum (black) of NGC 2865. The data have been binned using a bin-width of 0.3 Å for ease of visibility. Regions masked from the fit are the vertical areas, shaded gray. Bottom: residual percentage between the model and data. The 1σ uncertainty region is shown as the shaded gray region. (b) Same as Figure 2(a) but for NGC 3818. (c) Same as Figure 2(a) but for NGC 4915.

ATLAS3D galaxies (McDermid et al. 2015), the MaNGA survey galaxies (Gu et al. 2018; Parikh et al. 2021), and the nine galaxies studied in Feldmeier-Krause et al. (2021). We find that, as compared to these ETGs without fine structure, NGC 2865 has a stellar population that is younger relative to its determined velocity dispersion. None of the three ETGs, however, show any significant mass fraction (>15%) of a younger (<0.5 Gyr) stellar population.

We obtain a slightly subsolar to solar value in metallicity for all three ETGs, as can be seen in Figure 3. The abundance ratios of our reported elemental abundances are shown in Figure 4 as a function of velocity dispersion.

4.1.1. Carbon, Nitrogen, and Oxygen

C, N, and O are light elements formed in massive stars (O) and AGB stars (C and N), and are primarily determined in galaxies by ALF using molecular lines (e.g., CH, CN, TiO; Conroy et al. 2018). N is formed in intermediate-mass asymptotic giant branch (AGB) stars (unlike C, which is

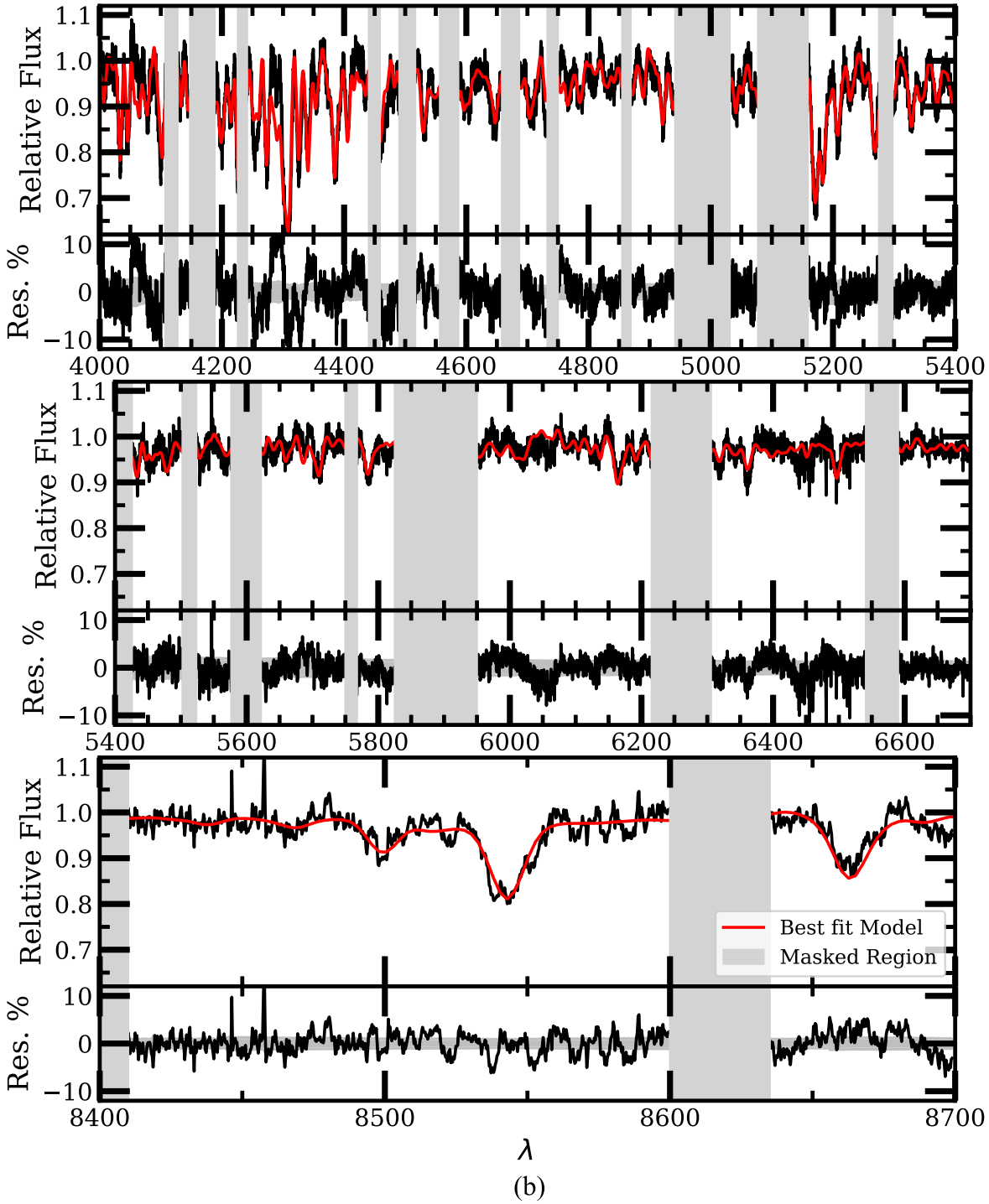

Figure 2. (Continued.)

produced in low-mass AGB stars), allowing stellar populations to be enriched in N earlier than C (Kobayashi et al. 2011).

All three ETGs are fit with a solar C abundance ([C/Fe] $\sim 0.0 \pm 0.1$), while the N and O median abundance ratios are slightly supersolar, at a [N,O/Fe] of $0.2-0.3 \pm 0.2$ dex.

4.1.2. α *Elements*

Mg, Si, Ca, and Ti (along with O) are produced in massive stars, and are ejected through CCSNe (Timmes et al. 1995; Kobayashi et al. 2006, 2020). Mg, Ti, and O affect large wavelength regions of the integrated-light spectra due to the TiO and MgH molecular absorption features present in the cooler and older stellar spectra that typically dominate in ETGs. The effect of these elements on the integrated-light spectra can be seen in the lower panels of the graphs in the figure set in the Appendix. The [α/Fe] ratio is used as a proxy for the star formation duration, with higher σ (i.e., more massive) galaxies showing larger [α/Fe] ratios (Thomas et al. 2005). However, outliers from the Mg–σ relationship have been shown to be caused by contribution from intermediate/young stellar populations within the ETGs (Thomas et al. 2005).

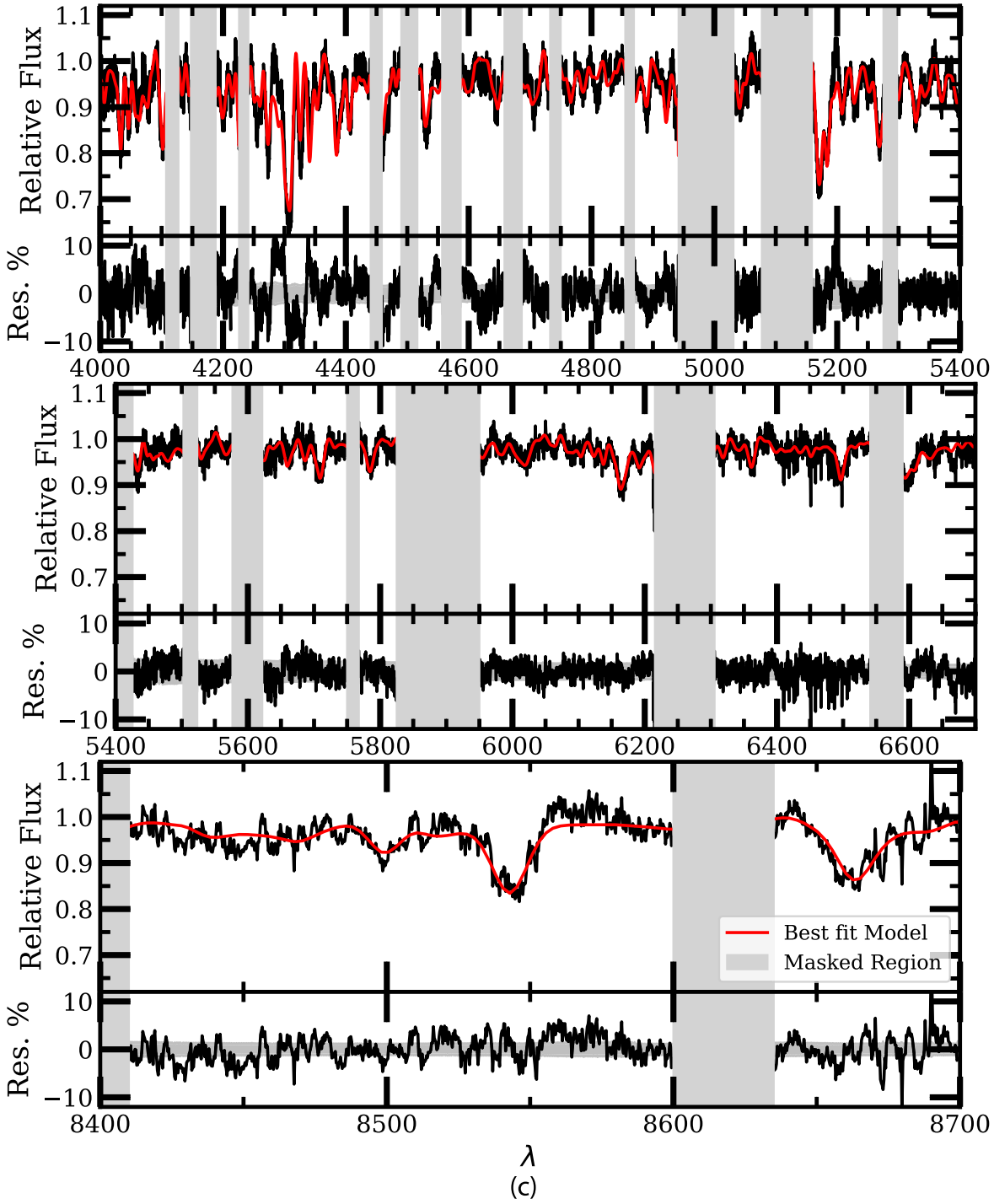

Figure 2. (Continued.)

The α elements vary slightly from C, N, and O in that NGC 2865 shows significant supersolar ([X/Fe] > 0.2) abundances for Mg, Si, and Ca, while the other two ETGs, NGC 3818 and NGC 4915, are supersolar in Mg but are determined to have solar Si and Ca abundances. Ti is determined to have significantly subsolar abundances for our three studied ETGs, particularly for NGC 3818. While Ti is expected to follow α elements like Si and Ca in abundances for ETGs, we do not observe this trend for our galaxies, in particular for NGC 3818. Near-infrared coverage of the TiO lines, which are unfortunately not covered by our spectra, are likely to allow a more robust test of the low Ti abundance, as described in Conroy et al. (2018).

4.1.3. Fe-peak Elements

The second group of elements that we fit using ALF are the Fe-peak elements, Fe, Cr, Mn, Co, Ni, and Cu. The Fe-peak elements generally follow the same trends as Fe, and often have many lines that affect the entire spectrum (Conroy et al. 2014). Cr and Mn are produced in the incomplete Si-burning regions of Type Ia SNe. Mn is produced in larger quantities than Fe

Table 3
Parameters of the Best-fit Model Shown in Figures 2(a)–(c) for NGC 2865, NGC 3818, and NGC 4915

Parameter	NGC 2865	NGC 3818	NGC 4915
σ (km s^{-1})	150 ± 9	179 ± 8	190 ± 17
Age (Gyr)	3.9 ± 1.3	7.3 ± 1.4	6.0 ± 1.5
Age of young SSP (Gyr)	1.4 ± 1.5	1.4 ± 1.5	1.3 ± 1.6
log (Mass % of young SSP)	-3.2 ± 1.3	-3.1 ± 1.2	-3.1 ± 1.3
[Fe/H]	-0.1 ± 0.1	0.0 ± 0.1	0.0 ± 0.1
[O/Fe]	0.2 ± 0.3	0.0 ± 0.3	0.1 ± 0.3
[C/Fe]	0.0 ± 0.1	0.0 ± 0.1	0.0 ± 0.2
[N/Fe]	0.1 ± 0.2	0.2 ± 0.2	0.0 ± 0.3
[Mg/Fe]	0.4 ± 0.2	0.4 ± 0.1	0.3 ± 0.2
[Si/Fe]	0.2 ± 0.2	0.0 ± 0.2	0.0 ± 0.3
[Ca/Fe]	0.3 ± 0.1	-0.1 ± 0.1	0.0 ± 0.1
[Ti/Fe]	-0.2 ± 0.2	-0.4 ± 0.2	0.0 ± 0.3
[Cr/Fe]	0.2 ± 0.1	0.0 ± 0.1	0.0 ± 0.2
[Mn/Fe]	0.3 ± 0.2	0.2 ± 0.2	0.1 ± 0.2
[Co/Fe]	0.1 ± 0.2	0.1 ± 0.2	0.0 ± 0.3
[Ni/Fe]	0.0 ± 0.2	0.0 ± 0.2	-0.1 ± 0.3
[Cu/Fe]	0.1 ± 0.3	0.0 ± 0.3	0.0 ± 0.3
[Sr/Fe]	0.1 ± 0.3	0.1 ± 0.3	0.0 ± 0.4
[Ba/Fe]	0.0 ± 0.3	0.0 ± 0.3	0.0 ± 0.4
[Eu/Fe]	0.1 ± 0.3	0.1 ± 0.3	0.0 ± 0.4

Note. We report values and uncertainties corresponding to the median and standard deviation of parameter values determined through our bootstrap fits.

leading to a positive [Mn/Fe] ratio with more Type Ia SNe, while Cr is produced near the same amount as Fe (Kobayashi et al. 2020). Moreover, the increase of [Co/Fe] at higher velocity dispersion in the Conroy & van Dokkum (2012b) data is speculated to be from Co enrichment from massive stars. Ni is produced in similar quantities to Fe (Kobayashi et al. 2020), however large abundance changes in Ni and Co do not produce significant spectral line changes, making both elements difficult to detect (see Figure 4 in Conroy et al. 2014).

The Fe-peak elements produce weaker features in integrated-light spectra than the lighter CNO and α elements. In NGC 2865 we find significant supersolar values of Cr ($[\mathrm{Cr/Fe}] = 0.22 \pm 0.14$) and Mn ($[\mathrm{Mn/Fe}] = 0.32 \pm 0.19$), and solar abundances within uncertainties for Co, Ni, and Cu. NGC 3818 and NGC 4915 have solar abundance ratios of Cr, Mn, Ni, and Cu. Interestingly, NGC 2865 shows the largest abundance of Cr out of the 3 ETGs, and while the dominant Cr yield is from Type Ia Sne, there is a non-negligible amount of Cr produced in Type II SNe (Kobayashi et al. 2011). NGC 2865 is enriched in both Mn and Cr, while NGC 3818 and NGC 4915 show no enrichment of Cr.

4.1.4. Neutron-capture Elements

Additionally, we use ALF to determine abundances for the neutron-capture elements Sr, Ba, and Eu. Elements such as Ba are produced in intermediate- and low-mass AGB stars through the slow neutron-capture process (*s*-process; Conroy et al. 2013). Rapid neutron-capture process (*r*-process) elements, such as Eu, are produced in dense neutron environments such as neutron star mergers (NSMs) and Type II CCSNe (Kobayashi et al. 2020). Determining the abundances of the *r*-process element Eu, while difficult to detect due to the faint nature of its spectral absorption features in stellar spectra, would allow for constraints on the rate of NSMs/CCSNe within ETGs, and the impact these events have on a galaxy.

The neutron-capture elements produce subtle and isolated responses in the integrated spectra of ETGs due to the weak nature of the lines in stellar spectra, unlike some of the lighter elements that affect broad wavelength regions (Conroy et al. 2013). As a result, the abundances of these elements are difficult to fit as the response is often lost in the noise of the spectra or in the broadening of nearby, stronger spectral features. In Figure 5, we show a sample of the distribution of fits from our bootstrap analysis to areas of the spectrum that are affected by C, Mg, Ba, Sr, and Eu. As stated in Section 4.2, the uncertainty in our determined abundance corresponds to the spread of fitted abundances ratios from our bootstrap analysis. In the Appendix we show the regions that each element affects for our observed wavelength range. For lighter elements such as C and Mg, we report smaller uncertainties because of the elements' strong contribution to the spectra and reliability of models with respect to those elements. For each of the three ETGs the median abundance of the bootstrap fitting for Sr, Ba, and Eu was solar, which suggests that the slightest changes to the regions of the integrated-light spectra that are affected by Sr, Ba, and Eu can produce large changes in the determined abundances. However, we discuss the implications of our determined abundances for Sr, Ba, and Eu to show how they relate to our interpretation of ETG chemical evolution.

We present a first-order determination of Eu, for the first time, from integrated-light spectra of distant galaxies. We note that the Eu lines are very weak in our spectra, which is reflected in the large error bars $\sim$0.5 dex. Each of our three ETGs with fine structure were determined to have an $[\mathrm{Eu/Fe}] \sim 0$. Such values were predicted in simulation work done by Naiman et al. (2018) which showed that Milky Way–type galaxies at $[\mathrm{Fe/H}] \sim 0$ have an [Eu/Fe] abundance of $\sim$0. We note that their simulations include merger events. The lack of enhancement or depletion postmerger, as signified by a $[\mathrm{Eu/Fe}] \sim 0$, indicate that either Eu and Fe were both equally produced during the merger or that one of the elements was overproduced in a manner that brought the [Eu/Fe] closer to zero.

4.2. Parameter Uncertainty

ALF provides uncertainties for each fit parameter using the shape of the posterior probability distribution created during the MCMC fitting routine. However, we found that the output from ALF provided uncertainties that did not reflect the true magnitudes of the total uncertainties in fitting the integrated-light spectra. In order to provide a more robust uncertainty for each parameter, we determine uncertainties for each of the fit parameters using a bootstrap method.

We generate 1000 spectra by drawing from a normal distribution centered on the original data spectrum for each galaxy, with a standard deviation equal to the uncertainty obtained in the data-reduction pipeline. Each spectrum is then fit using the same fitting routine to obtain 1000 sets of parameter values for each galaxy. Figure 5 shows a sample of fitted models for different regions of the galaxy spectra, which demonstrates the spread in model fits with our spectra. In Table 3, we report the median value, and the uncertainty corresponds to the standard deviation of the distribution of the set of parameter values obtained in the bootstrap analysis. For the chemical abundances, our uncertainties range from $\sim$0.1 to 0.4 dex, with the lighter elements (C, N, O, Mg, Si,

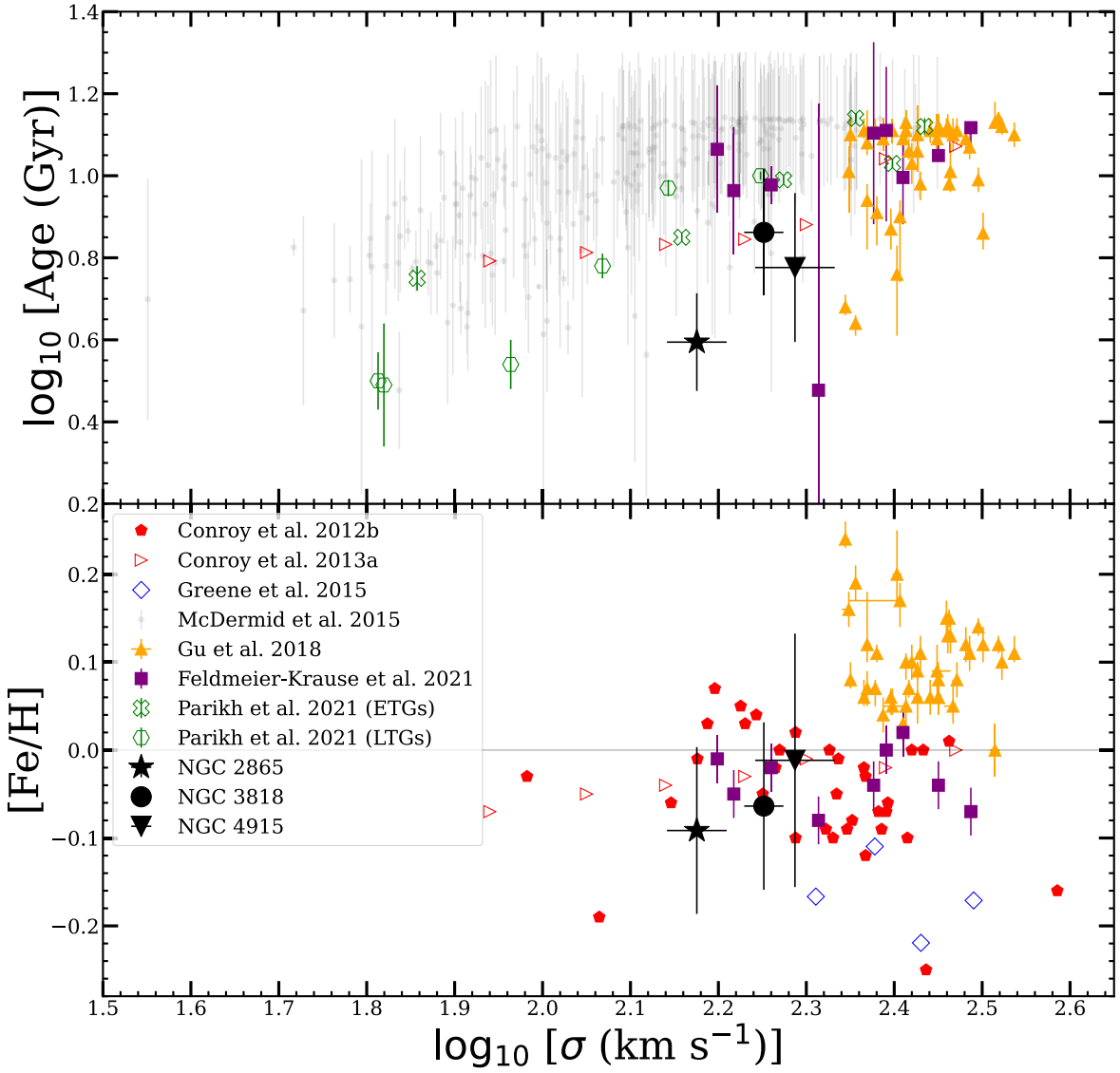

Figure 3. Relationship between the velocity dispersion and the age and [Fe/H] for NGC 2865 (black star), NGC 3818 (black circle), and NGC 4915 (black square). Ages and metallicities determined from Conroy & van Dokkum (2012b, filled red pentagons), Conroy et al. (2014, unfilled red triangles), Greene et al. (2015, unfilled blue diamonds), McDermid et al. (2015, gray dots), Gu et al. (2018, filled orange triangles), Feldmeier-Krause et al. (2021, filled purple squares), and Parikh et al. (2021, unfilled X's for ETGs, unfilled hexagons for LTGs) are included for comparison. Filled-in markers represent results determined for individual galaxies, while open markers correspond to results derived from stacked data over discrete mass bins. A horizontal black line is shown for solar metallicity ([Fe/H] = 0) in the bottom plot. The central regions of our three ETGs show younger ages than most other ETGs of the same σ, especially in the case of NGC 2865.

Ca, and Ti) generally having smaller uncertainties than the heavier elements (Cr, Mn, Co, Ni, Cu, Sr, Ba, and Eu).

5. Comparison to Early-type Galaxies without Fine Structure

We compare our results to other spectroscopic galaxy surveys that use full-spectrum fitting in order to study the relation between fine-structure content and the chemical abundance ratios in ETGs. The first of our literature sources is the work done in Conroy & van Dokkum (2012b), Conroy et al. (2014, 2013), and Conroy et al. (2018), from which the ALF fitting routine originated. Their work uses stacked SDSS observation to obtain high-SNR spectra for discrete velocity dispersion bins of ETGs. In Conroy & van Dokkum (2012b), they examine 34 ETGs from the SAURON survey (Bacon et al. 2001; de Zeeuw et al. 2002). We also compare our work to the ATLAS3D survey of ETGs (Cappellari et al. 2010), which includes a star formation history and stellar population study done in McDermid et al. (2015). Gu et al. (2018b) also uses ALF to study stacked spectra taken from the MaNGA survey (Bundy 2015; Drory et al. 2015; Yan et al. 2016; Wake et al. 2017; Abolfathi et al. 2018), specifically ETGs in the Coma Cluster. Additionally from the MaNGA survey, Parikh et al. (2021) uses stacked spectra to study gradients using line indice models to obtain ages, chemical abundances, and kinematic information. Their work uniquely studies not only ETGs but select late-type galaxies (LTGs), as well, which allows comparisons of our sample of recently merged galaxies with other galaxy types. We compare to Greene et al. (2015), which uses galaxies from the MASSIVE survey (Ma et al. 2014), and which is a volume-limited survey that excludes large spiral and interacting galaxies. Finally, we include results from Feldmeier-Krause et al. (2021), which obtained abundance ratios for eight ETGs and one low-surface-brightness spiral galaxy using

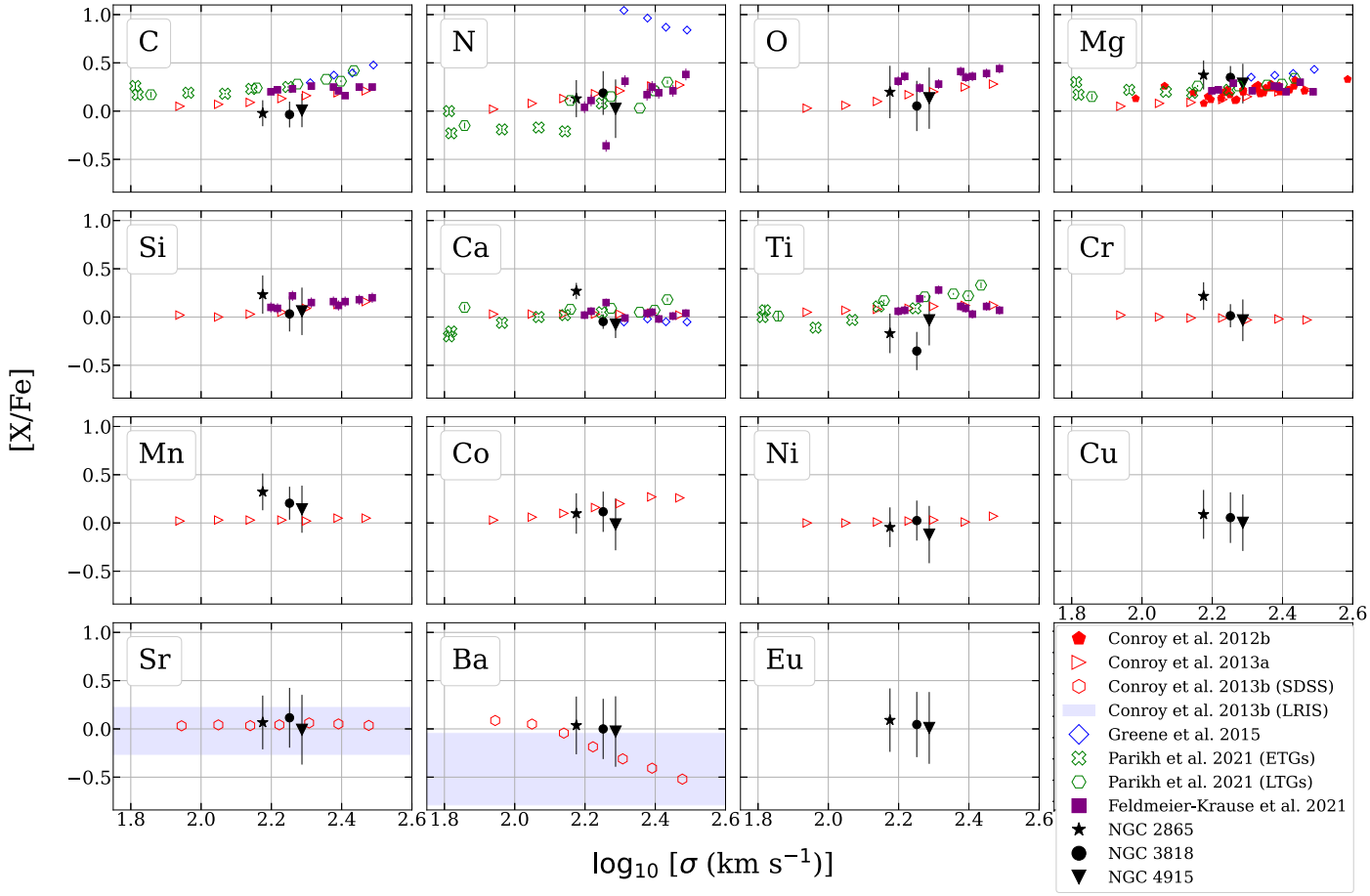

Figure 4. [X/Fe] ratio for NGC 2865 (black stars), NGC 3818 (black circles), and NGC 4915 (black squares) are plotted against the galaxies' central velocity dispersion and compared to literature abundances of Conroy & van Dokkum (2012b, filled red pentagons), Conroy et al. (2014, unfilled red triangles), Conroy et al. (2013, unfilled red hexagons), Greene et al. (2015, unfilled blue diamonds), Feldmeier-Krause et al. (2021, filled purple squares), Parikh et al. (2021, unfilled X's for ETGs, unfilled hexagons for LTGs). Sr and Ba are determined for individual galaxies in Conroy et al. (2013); however, the velocity dispersions are not reported. We instead show the range of abundances covered by their results as the light blue shaded region. The abundances plotted correspond to the values and uncertainties reported in Table 3. Filled-in markers represent results determined for individual galaxies, while open markers correspond to results derived from stacked data over discrete mass bins.

full-spectrum fitting methods. Many of the surveys explore gradients, and thus report abundances for various radii from the galactic center. For the purpose of this study, we only compare to the literature results at the center of each system.

5.1. Velocity Dispersions and Ages

The velocity dispersion, σ, is a proxy for the galaxy mass, with higher σ correlating with more massive galaxies (Faber & Jackson 1976). As can be seen in Figure 3, more massive galaxies tend to be dominated by older stellar populations (McDermid et al. 2015; Gu et al. 2018; Feldmeier-Krause et al. 2021). As shown in Figure 3, NGC 2865 shows younger stellar populations than most of the galaxies in its mass range (with the exception of a few other outliers), while NGC 3818 and NGC 4915 are determined to have ages that are similar to other ETGs of similar mass ranges, within uncertainties. It is possible that the merger events of NGC 2865 produced periods of star formation from which there are more young stars contributing to the integrated light (Hopkins et al. 2008).

5.2. Chemical Abundance Comparisons

Elements that produce strong features in ETG spectra, such as C, N, Mg, Ca, and Ti, have been measured in many surveys (Conroy & van Dokkum 2012b; Greene et al. 2015; Feldmeier-Krause et al. 2021; Parikh et al. 2021). To reach the SNR needed (SNR >100; Conroy & van Dokkum 2012b) to measure elements such as Cr, Mn, Co, Ni, Cu, Sr, Ba, and Eu, surveys often bin ETGs into discrete mass bins and coadd the low-SNR spectra. As a result, Fe-peak elements are less reported than the lighter elements, and we are limited to comparisons to Conroy & van Dokkum (2012b). There are no galaxies with reported abundances for some heavy elements, such as Cu and Eu.

We find that the three ETGs have median [C/Fe] derived abundances of about 0.1–0.2 dex lower than literature ETGs. While our C abundances are lower than the trend established by the literature ETGs, the result may be unsurprising as we see slightly supersolar N abundances. At metallicities of [Fe/H] > -0.2 dex, Maiolino & Mannucci (2019) show that N may be produced as a secondary element from intermediate stars already enhanced in C and O, which could result in a higher N abundance and a lower C abundance following a burst of star formation. Furthermore, Conroy et al. (2014) show that N tracks O very closely, while C does not at higher velocity dispersions ($\log \sigma > 2.1$ km s^{-1}). Similar to N, all three ETGs are determined to have [O/Fe] ratios that lay in the same abundance range as the literature ETGs.

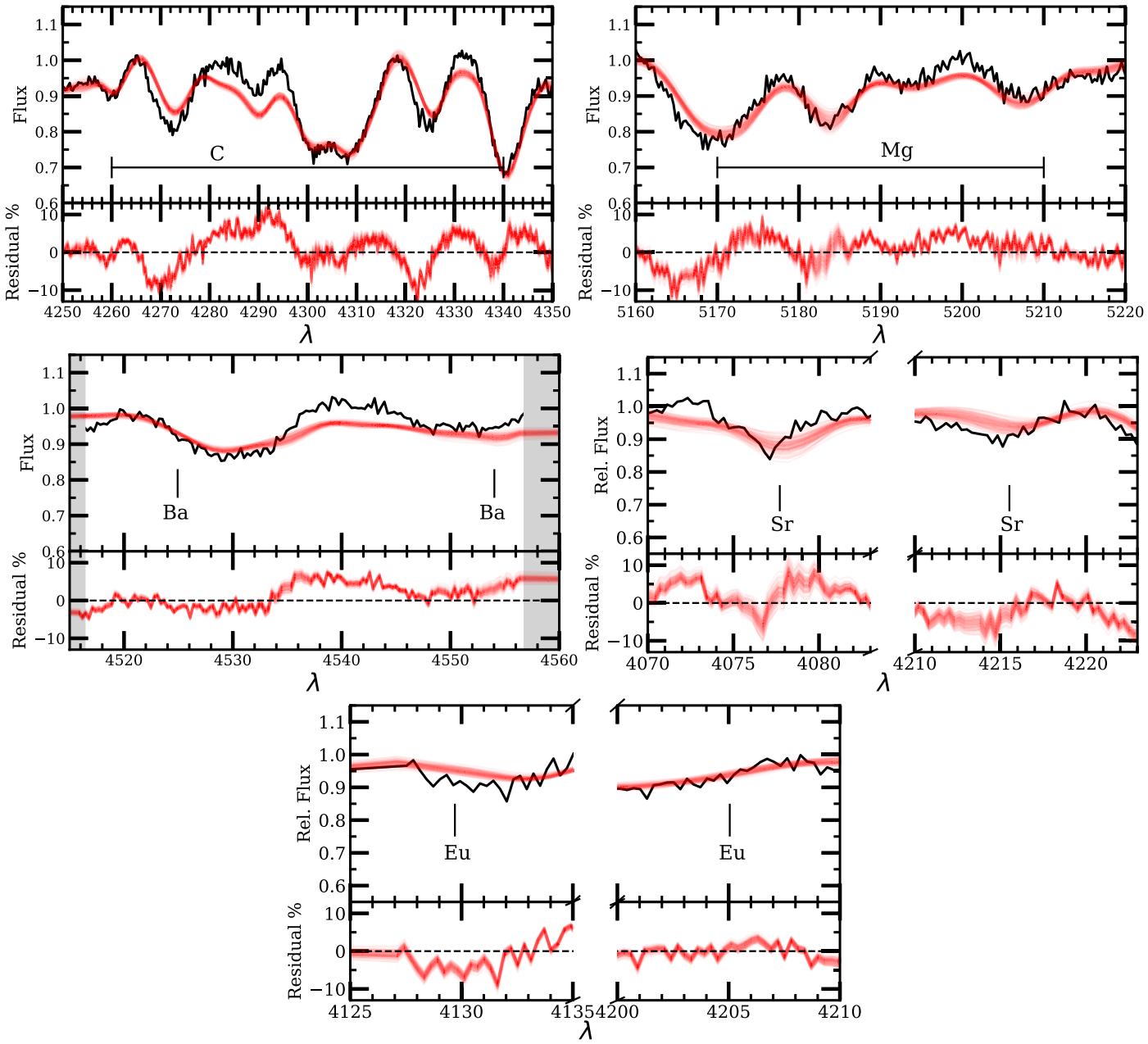

Figure 5. Fits from our bootstrap analysis are overlayed for NGC 2865 for sections of the spectrum that are influenced by C (top-left panel), Mg (top-right panel), Ba (middle-left panel), Sr (middle-right panel), and Eu (bottom panel). The top graph of each panel displays a random sample of 100 of the 1000 model spectra fits as red lines, while the original data spectrum of NGC 2865 is in black. The bottom graph of each panel shows the residual percentage from each model spectrum and the data spectrum.

Mg is a well-studied element in ETGs, as it produces strong and localized spectral lines that contribute to the integrated-light spectrum (as can be seen in the bottom panel of Figure 8.4 in the Appendix). As can be seen in Figure 4, all three of our ETGs lie close to or on the observed literature ETG [Mg/Fe] abundance values. We also find similar abundances within uncertainty for Si to the literature ETGs. However, with the [Ca/Fe] abundance, we find that NGC 2865 has a significantly higher [Ca/Fe] abundance when compared to ETGs of a similar velocity dispersion, while NGC 3818 and NGC 4915 have abundances that lie near the literature ETG abundances. As mentioned in Section 4.1.2, the α elements are formed through the stellar evolution of massive stars (Kobayashi et al. 2020). The [α/Fe] is observed to decrease at [Fe/H] > -1 due to increased Fe contributions from Type Ia SNe.

As Conroy et al. (2014) uses stacked σ bins, we do not know the scatter for Cr, Mn, Co, and Ni in each σ bin. However, their measurements show trends as the galaxies grow in mass for the Fe-peak elements. Cr, Mn, Ni remain near solar ([X/Fe] ~ 0) for all mass bins, as these elements are produced in the same processes that produce Fe. Co, an element thought to form in massive stars, does break this trend by increasing in [Co/Fe] with increasing σ. The three ETGs studied in this work generally lie around the trends seen in Conroy et al. (2014), however we find that NGC 2865 lies above the results of Conroy et al. (2014) in Cr and Mn. As noted in Section 4.1,

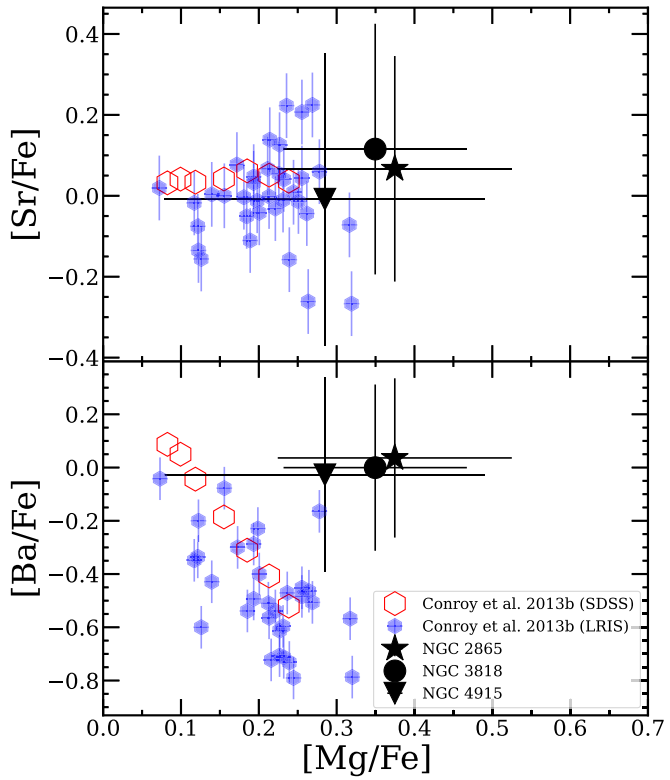

Figure 6. [Sr/Fe] (upper panel) and [Ba/Fe] (bottom panel) abundance ratios of this work (NGC 2865, stars; NGC 3818,circles; NGC 4915, triangles) compared to results presented in Conroy et al. (2013, filled light blue hexagons for LRIS individual galaxies, and unfilled red hexagons for stacked SDSS data) for ETGs. We see agreement for the [Sr/Fe] trend, but we do not observe a decreasing [Ba/Fe] trend found in Conroy et al. (2013).

NGC 2865 being enhanced in Cr and Mn could be a result of a rapid enrichment, possibly due to the merger event, where Type Ia SNe could not occur quick enough to inject Fe into the ISM and lower the abundance ratios with respect to Fe. We find a solar [Ni/Fe] ~ 0 ratio for NGC 2865, which does not follow the the other Fe-peak elements (like Cr, Mn, and Co). The solar value of [Ni/Fe] is consistent with chemical evolution models and observations of stars at a [Fe/H] > -1. Ni and Fe are both produced in the complete Si-burning region of a star, which makes the the [Ni/Fe] ratio unaffected by multiple periods of star formation (Kobayashi et al. 2020). The production of Mn and Cr, on the other hand, are produced in the incomplete Si-burning region, and could thus have been enhanced relative to Fe during bursts of star formation, as observed in NGC 2865, due to material ejection during SNe (Kobayashi et al. 2020).

Conroy et al. (2013) reports abundances for Sr and Ba in ETGs for both stacked SDSS spectra and low-resolution spectra for individual galaxies. We show our results compared to Conroy et al. (2013) in Figure 6, where the Sr and Ba abundance ratios are plotted for ETGs with respect to their [Mg/Fe] ratios. The decreasing [Ba/Fe] trend with respect to the [Mg/Fe] abundance probes the timescale of star formation within the ETG, with shorter timescales leading to higher [Mg/Fe] values and lower [Ba/Fe] values (Conroy et al. 2013). The three ETGs studied in our work are determined to have solar abundances, which agrees with the Sr results of Conroy et al. (2013) but not the decreasing trend of Ba with increasing Mg.

6. Discussion

The abundance ratios shown in Figure 4 for previous ETG studies show the observed chemical abundances for quiescent galaxies for a given mass. We explore how the merger history of ETGs could have altered the chemical evolution history in these systems by modeling different merger scenarios. For example, a late ($z \leqslant 1$) disk–disk merger would experience a large fraction (up to 40%) of in situ star formation in the central region of the merger remnant (Barnes & Hernquist 1996; Naab et al. 2014). As the two progenitor galaxies merge, early dissipation and inflows of gas from the parent galaxies cause an increased star formation rate during the first pass of the merger (Mihos & Hernquist 1996). The stars formed in this phase of the merger are in general massive and hence enrich the ISM gas on a timescale of $\sim$20 Myr. These massive stars then quickly inject α elements and Fe-peak elements such as Cr, Mn, Co into the ISM.

6.1. NGC 2865

NGC 2865 contains the most fine structure out of our three ETGs, with a fine-structure constant of $\Sigma = 6.4$. We note that NGC 2865, which is the only galaxy to show statistically higher Ca, Mn, and Cr abundances compared to ETGs without fine structure, is the youngest, least massive, and most recently perturbed system out of our three ETGs. We explore possible physical explanations that would lead to enhancement of certain α and Fe-peak elements.

Simulations of major mergers suggest that there are two periods of intense star formation during the galaxy-pair interaction, one occurring during the first pass of the progenitor galaxies, and the second occurring during coalescence (Moreno et al. 2019, 2021). We test if a simple two-burst model would be sufficient in explaining the differences in abundances for NGC 2865 compared to other ETGs without fine structure using the Starburst99 program (SB99; González Delgado et al. 1999; Vázquez & Leitherer 2005; Leitherer et al. 2010, 2014). SB99 outputs yields of some elements as a function of gas cloud mass, IMF parameters, and time. We use SB99 to model the predicted elemental yields as a function of time after a single burst star formation event. We model this by assuming an initial ISM at solar metallicity with default SB99 parameters (IMF, cutoff, etc.) and plot the resulting metallicity of the gas, assuming fill mixing of the enriched gas predicted by SB99 yields. We show the [X/Fe] abundance ratios of gas clouds modeled by SB99 in Figure 7 for C, N, O, Mg, and Si. We find that there is not enough time for stars born during the starburst periods of a merger to both significantly contribute to the light output of the galaxy and to have abundances similar to what we determine for NGC 2865. The discrepancy between our abundances for the α elements and the abundances modeled in SB99 suggests that a simple two-burst model scenario cannot fully capture the chemical evolution taking place before or after a major merger event. Additional environmental components such as other periods of starburst activity, chemically peculiar progenitor galaxies, or accretion of chemically enriched satellite galaxies into the central regions of merger remnants could be the cause of the abundance offsets seen in NGC 2865.

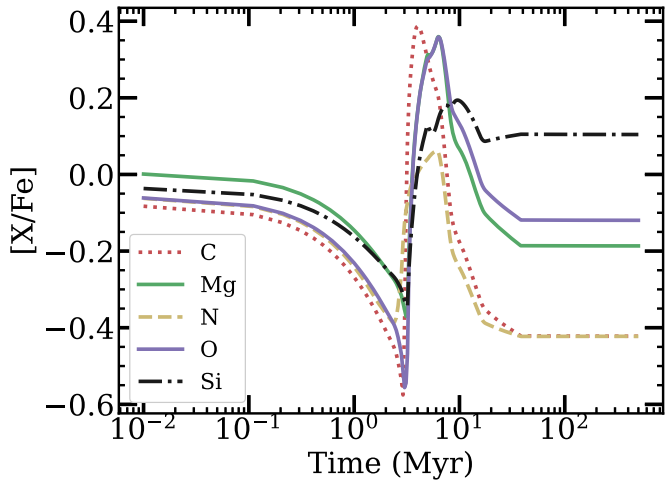

Figure 7. Chemical abundances as a function of time for a gas cloud with an initial solar metallicity using the Starburst99 program (SB99; González Delgado et al. 1999, Vázquez & Leitherer 2005; Leitherer et al. 2010, 2014). The abundances displayed are derived using the yields modeled by SB99 for a gas cloud with a mass comparable to NGC 2865.

6.2. NGC 3818

NGC 3818 does not show any abundance differences to ETGs without fine structure. NGC 3818 experienced its major merger earlier than NGC 2865, and which could explain the agreement of [α/Fe] ratios to ETGs without fine structure. The fine-structure constant of NGC 3818 is the lowest of the three ETGs studied in this work, at $\Sigma = 1.3$ In the case of NGC 3818, its main fine-structure feature is a boxy isophote with an embedded disk, which are both structures associated with high-mass, gas-poor (dry) mergers (Giri et al. 2023). If the fine structure was formed in a dry merger, then we would expect a lack of chemical differences to ETGs without fine structure, as there would have been little-to-no star formation during the merger. The abundances we observe in NGC 3818 demonstrate that its dry merger event did not chemically alter the system.

6.3. NGC 4915

Finally, in the case of NGC 4915, we find chemical abundance ratios similar to NGC 3818 and other ETGs. However, NGC 4915 is fit with a younger stellar population (relative to other ETGs of a similar mass) at its center and it possesses a fine-structure constant of $\Sigma = 5.5$. Schweizer et al. (1990) suggests that NGC 4915 was a product of a disk–disk merger, and if NGC 4915 experienced enough gas inflow to the center of the galaxy spurring star formation, it would explain the presence of a younger stellar population. Assuming that the stellar and gaseous abundance patterns are the same in the progenitor galaxies that formed NGC 4915, the gas present at the time of the merger was likely chemically similar to the gas found in ETGs without fine structure at the same epoch. As a result, the resulting stellar population that formed during the merger would then be chemically similar to that of ETGs without fine structure.

6.4. Chemical Abundances and Fine Structure

While the fine-structure constant, Σ, is a useful measurement of how disturbed a system is, the three ETGs here show that its value does not indicate a level of chemical enrichment. NGC 3818 and NGC 4915, the two ETGs whose fine structure mostly comes from their boxy isophotes, show little chemical differences to ETGs without fine structure. However, NGC 2865, which possesses tidal tails and extended shells, shows offsets in the α and Fe-peak elements when compared to ETGs without fine structure. As mentioned in Section 1, NGC 2865's shells resemble disk galaxies in color as a result of disk–disk galaxy merger, therefore the younger, blue populations of the shells may be linked to the younger stellar populations observed at the center of NGC 2865. NGC 3818's and NGC 4915's lack of abundance to ETGs without fine structure, compared to the chemical offset seen in NGC 2865, could indicate that the type of fine structure (i.e., boxy isophotes versus stellar streams and shells) present around a merger remnant correlates with the chemical composition of the merger remnant.

7. Conclusions

We present elemental abundance ratios for three early-type elliptical galaxies that have fine structure. The chemical compositions derived from their nuclear spectrum offers a unique look into if and how the stellar populations at the center of ETGs are affected by major mergers. After comparing our ETGs with fine structure to literature ETGs without detected fine structure, we offer the following conclusions:

1. We present the derived abundance ratios for a wide array of elements including C, N, O, Mg, Si, Ca, Ti, Cr, Mn, Co, Ni, Cu, Sr, Ba, and Eu. We conduct a bootstrap analysis to probe the reliability of the determined abundances and find that the heavier elements like Cu, Sr, Ba, and Eu are subject to larger uncertainties due to their small response functions and ability to be blended with stronger, nearby elements. Therefore, it is imperative to maximize the SNR in spectra and improve our understanding of the response functions of heavy elements and refining our stellar library models if we want to better constrain their abundances.
2. Among the three galaxies we analyzed in this paper, only NGC 2865 shows a chemical difference to literature galaxies without fine structure. We determine that an ETG having fine structure does not necessarily mean its abundance pattern will differ from other ETGs of similar mass.
3. We attribute the abundances differences found in NGC 2865 to the star formation that occurred during its last major merger. The higher derived abundance ratios in NGC 2865 for Ca, Cr, and Mn as compared to ETGs without fine structure could suggest a more complex star formation history than a simple, two-burst scenario. A more complex scenario would be necessary to characterize NGC 2865's star formation history (SFH), and would have to consider other merger variables such as the effects of gas inflows and outflows during the merger. Additionally, a more complex SFH could explain why some of the elements such as Ca, Cr, and Mn are enriched, while other elements in the same nucleosynthesis family are not.

Our study of the chemical abundances at the center of ETGs with fine structure has revealed that the presence of fine structure alone does not imply a chemical difference for the stellar populations, however there is evidence that the type of fine structure and the variations in abundance patterns may be a consequence of the same event, the merger and associated star

formation. Future chemical abundance studies, especially integral field spectroscopy (IFS) to derive abundance gradients from the center to the outer regions of ETGs with fine structure, will be a valuable tool in determining the extent to which the type of fine structure alters the chemical abundances. IFS spectra of ETG regions associated with types of fine structure seen in NGC 2865 (shells, tidal streams), can be compared to the spectra obtained from regions without fine structure in the same galaxy. This comparison will show how the type of fine structure correlates with abundances, and furthermore the chemical evolution history associated with different types of fine structure.

Acknowledgments

The authors acknowledge University of Florida Research Computing for providing computational resources and support that have contributed to the research results reported in this publication (http://researchcomputing.ufl.edu).

We thank Charlie Conroy not only for his Absorption Line Fitter program, but also his assistance on improving the fit using the high-resolution MIKE data.

N.B. acknowledges support from the NASA Future Investigators in NASA Earth and Space Science and Technology (FINESST) Grant 21-ASTRO21-0075.

R.E. acknowledges support from NSF grant No. AST-2206263.

The National Radio Astronomy Observatory is a facility of the National Science Foundation operated under cooperative agreement by Associated Universities, Inc.

E.T. acknowledges support from ANID through Millennium Science Initiative Program – NCN19_058, CATA-BASAL – ACE210002 and FB210003, FONDECYT Regular – 1190818 and 1200495.

Facility: Magellan:Clay (MIKE spectrograph).

Software: Absorption Line Fitter (ALF)—(Conroy & van Dokkum 2012b; Conroy et al. 2018), Python (Van Rossum & Drake 2009), CarPy (Kelson et al. 2000; Kelson 2003), Astropy (Astropy Collaboration et al. 2022), Numpy (Harris et al. 2020), Scipy (Virtanen et al. 2020), Matplotlib (Hunter 2007).

Appendix
Detailed Results

In order to evaluate the fit of each individual element by ALF, we produce plots that display characteristics of the fitting routine. For each element, we display the median fitted abundance ratio compared to other ETGs (top-left panel in each figure), the distribution of fitted values for that element from our bootstrap analysis (top-right panel), the parameter covariance between the element and other fitted parameters of ALF (middle-row panel), and finally the response function (what wavelength regions the element affects) of the element (bottom-row panel).

In the subfigures of Figure 8, we compare our abundance ratios to ETG studies by Conroy & van Dokkum (2012b), Conroy et al. (2014, 2013), Greene et al. (2015), Feldmeier-Krause et al. (2021), and Parikh et al. (2021). The colors and symbols used for the literature samples are consistent with Figure 4. We compare literature sources that also use full-spectrum fitting methods in order to provide a consistent comparison sample.

The parameter covariance is shown by the correlation coefficients graph. Parameters that show a strong correlation indicate that when ALF produces a model with the selected parameter at a certain value, other parameters that correlate are typically fit with similar trends (e.g., a large O abundance model often has a large C abundance as well).

We include the response function of each element to show the areas of the spectra that are most affected by changes in the specified element. The response function is constructed by taking two models generated by ALF, with all of the same parameter values except for that of the element of interest. The difference between these two models thus shows where the spectra change when there is a difference abundance ratio present. We use the response function to determine if we are fitting the strongest regions of the spectra for that particular element.

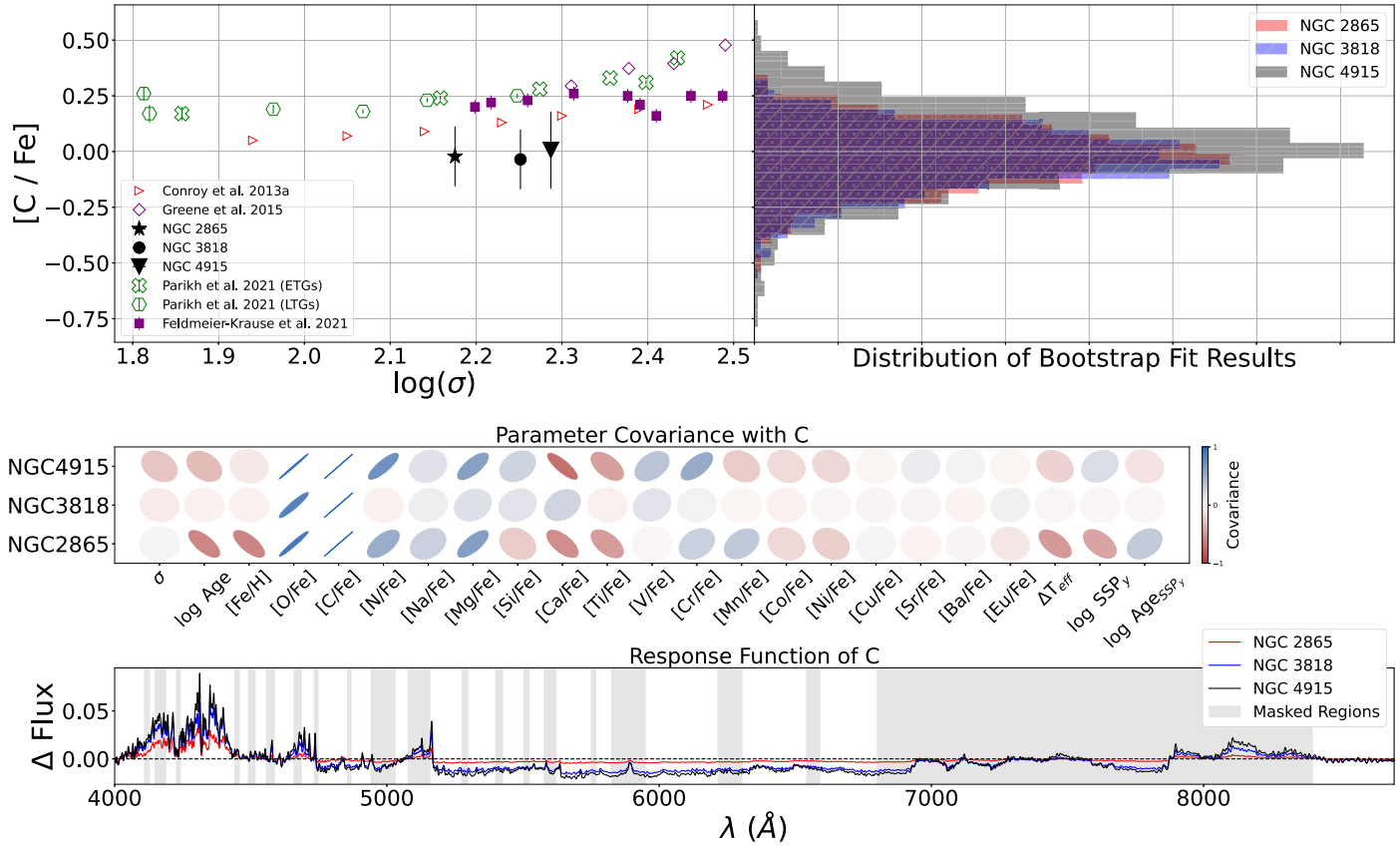

Figure 8. Determinations of carbon abundance in each ETG. Top-left panel: Comparison of [C/Fe] abundance ratios to literature ETGs plotted against the velocity dispersion. Top-right panel: Distribution for the carbon abundance from 1000 fitting routines run over spectra sampled from our observed spectrum. The MCMC routine utilized 1024 walkers and a chain of 10,000 after the burn-in. Middle panel: parameter covariance of carbon compared to the other parameters in the fit (blue, right-leaning ovals indicate a strong correlation; red, left-leaning ovals indicate anticorrelation; and round, pale ellipses indicate no correlation). Bottom panel: difference between two models synthesized with [C/Fe] ratios ±0.5 dex above and below the median of the [C/Fe] posterior distribution. Areas of the spectrum that deviate from zero show where carbon has an effect on the integrated light.

(The complete figure set (15 images) is available.)

ORCID iDs

Nicholas Barth https://orcid.org/0000-0003-0602-5287
George C. Privon https://orcid.org/0000-0003-3474-1125
Rana Ezzeddine https://orcid.org/0000-0002-8504-8470
Aaron S. Evans https://orcid.org/0000-0003-2638-1334
Ezequiel Treister https://orcid.org/0000-0001-7568-6412

References

Abolfathi, B., Aguado, D. S., Aguilar, G., et al. 2018, ApJS, 235, 42
Astropy Collaboration, Price-Whelan, A. M., Lim, P. L., et al. 2022, ApJ, 935, 167
Bacon, R., Copin, Y., Monnet, G., et al. 2001, MNRAS, 326, 23
Barnes, J. E., & Hernquist, L. 1996, ApJ, 471, 115
Bensby, T., Feltzing, S., & Oey, M. S. 2014, A&A, 562, A71
Bernstein, R., Shectman, S. A., Gunnels, S. M., Mochnacki, S., & Athey, A. E. 2003, Proc. SPIE, 4841, 1694
Bundy, K. 2015, in IAU Symp. 311, Galaxy Masses as Constraints of Formation Models, ed. M. Cappellari & S. Courteau (Cambridge: Cambridge Univ. Press), 100
Cappellari, M., Emsellem, E., Krajnovic, D., et al. 2010, MNRAS, 413, 813
Chambers, K. C., Magnier, E. A., Metcalfe, N., et al. 2016, arXiv:1612.05560
Conroy, C., Graves, G., & van Dokkum, P. 2014, ApJ, 780, 33
Conroy, C., & van Dokkum, P. 2012a, ApJ, 747, 69
Conroy, C., van Dokkum, P., & Graves, G. J. 2013, ApJL, 763, L25
Conroy, C., & van Dokkum, P. G. 2012b, ApJ, 760, 71
Conroy, C., Villaume, A., van Dokkum, P. G., & Lind, K. 2018, ApJ, 854, 139
de Vaucouleurs, G., de Vaucouleurs, A., Corwin, H. G. J., et al. 1991, Third Reference Catalogue of Bright Galaxies (New York: Springer)
de Zeeuw, P. T., Bureau, M., Emsellem, E., et al. 2002, MNRAS, 329, 513
Drory, N., MacDonald, N., Bershady, M. A., et al. 2015, AJ, 149, 77
Faber, S. M., & Jackson, R. E. 1976, ApJ, 204, 668
Feldmeier-Krause, A., Lonoce, I., & Freedman, W. L. 2021, ApJ, 923, 65
Fort, B. P., Prieur, J. L., Carter, D., Meatheringham, S. J., & Vigroux, L. 1986, ApJ, 306, 110
Fukazawa, Y., Botoya-Nonesa, J. G., Pu, J., Ohto, A., & Kawano, N. 2006, ApJ, 636, 698
Giri, G., Barway, S., & Raychaudhury, S. 2023, MNRAS, 520, 5870
González Delgado, R. M., Leitherer, C., & Heckman, T. M. 1999, ApJS, 125, 489
Greene, J. E., Janish, R., Ma, C.-P., et al. 2015, ApJ, 807, 11
Greif, T. H., Glover, S. C. O., Bromm, V., & Klessen, R. S. 2010, ApJ, 716, 510
Gu, M., Conroy, C., & Brammer, G. 2018, ApJL, 862, L18
Gu, M., Conroy, C., Law, D., et al. 2020, ApJ, 894, 32
Harris, C. R., Millman, K. J., van der Walt, S. J., et al. 2020, Natur, 585, 357
Hau, G. K. T., & Forbes, D. A. 2006, MNRAS, 371, 633
Hopkins, A. M., McClure-Griffiths, N. M., & Gaensler, B. M. 2008, ApJL, 682, L13
Hunter, J. D. 2007, CSE, 9, 90
Jorgensen, I., Franx, M., & Kjaergaard, P. 1992, A&AS, 95, 489
Kelson, D. D. 2003, PASP, 115, 688
Kelson, D. D., Illingworth, G. D., van Dokkum, P. G., & Franx, M. 2000, ApJ, 531, 137
Kobayashi, C., Karakas, A. I., & Lugaro, M. 2020, ApJ, 900, 179
Kobayashi, C., Karakas, A. I., & Umeda, H. 2011, MNRAS, 414, 3231
Kobayashi, C., Umeda, H., Nomoto, K., Tominaga, N., & Ohkubo, T. 2006, ApJ, 653, 1145

Kroupa, P. 2001, MNRAS, 322, 231
Leitherer, C., Ekström, S., Meynet, G., et al. 2014, ApJS, 212, 14
Leitherer, C., Ortiz Otálvaro, P. A., Bresolin, F., et al. 2010, ApJS, 189, 309
Longhetti, M., Bressan, A., Chiosi, C., & Rampazzo, R. 1998, A&AS, 130, 251
Ma, C.-P., Greene, J. E., McConnell, N., et al. 2014, ApJ, 795, 158
Maiolino, R., & Mannucci, F. 2019, A&ARv, 27, 3
McDermid, R. M., Alatalo, K., Blitz, L., et al. 2015, MNRAS, 448, 3484
Mihos, J. C., & Hernquist, L. 1996, ApJ, 464, 641
Milone, A. D. C., Sansom, A. E., & Sánchez-Blázquez, P. 2011, MNRAS, 414, 1227
Moreno, J., Torrey, P., Ellison, S. L., et al. 2019, MNRAS, 485, 1320
Moreno, J., Torrey, P., Ellison, S. L., et al. 2021, MNRAS, 503, 3113
Naab, T., Johansson, P. H., & Ostriker, J. P. 2009, ApJL, 699, L178
Naab, T., Oser, L., Emsellem, E., et al. 2014, MNRAS, 444, 3357
Naiman, J. P., Pillepich, A., Springel, V., et al. 2018, MNRAS, 477, 1206
Oser, L., Ostriker, J. P., Naab, T., Johansson, P. H., & Burkert, A. 2010, ApJ, 725, 2312
Panuzzo, P., Rampazzo, R., Bressan, A., et al. 2011, A&A, 528, A10
Parikh, T., Thomas, D., Maraston, C., et al. 2021, MNRAS, 502, 5508
Rampazzo, R., Marino, A., Tantalo, R., et al. 2007, MNRAS, 381, 245
Rawle, T. D., Smith, R. J., & Lucey, J. R. 2010, MNRAS, 401, 852
Schiavon, R. P. 2007, ApJS, 171, 146
Schweizer, F., & Seitzer, P. 1992, AJ, 104, 1039
Schweizer, F., Seitzer, P., Faber, S. M., et al. 1990, ApJL, 364, L33
Scorza, C., & van den Bosch, F. C. 1998, MNRAS, 300, 469
Smith, R. J., Lucey, J. R., Hudson, M. J., Schlegel, D. J., & Davies, R. L. 2000, MNRAS, 313, 469
Thomas, D., Maraston, C., Bender, R., & Mendes de Oliveira, C. 2005, ApJ, 621, 673
Timmes, F. X., Woosley, S. E., & Weaver, T. A. 1995, ApJS, 98, 617
Tully, R. B. 1988, Nearby Galaxies Catalog (New York: Cambridge Univ. Press)
Urrutia-Viscarra, F., Torres-Flores, S., Mendes de Oliveira, C., et al. 2017, A&A, 606, A77
Van Rossum, G., & Drake, F. L. 2009, Python 3 Reference Manual (Scotts Valley, CA: CreateSpace)
Vázquez, G. A., & Leitherer, C. 2005, ApJ, 621, 695
Virtanen, P., Gommers, R., Oliphant, T. E., et al. 2020, NatMe, 17, 261
Wake, D. A., Bundy, K., Diamond-Stanic, A. M., et al. 2017, AJ, 154, 86
Yan, R., Bundy, K., Law, D. R., et al. 2016, AJ, 152, 197